Journal of
Polymer Materials

Tech Science Press

http://doi.org/10.32604/jpm.2026.085943

ARTICLE

p-Phenylenediamine-Benzoquinone Polymer/Reduced Graphene Oxide Flexible Composite Films as a Cathode Material for Rechargeable Lithium-Ion Batteries

Zhouqishuo Cai[#], Donghua Liu[#], Yanan Zhao, Zewen Lin, Shumin Lin, Dan Zhong and Hua Bai[*]

College of Materials, Xiamen University, Xiamen, China
[*]Corresponding Author: Hua Bai. Email: baihua@xmu.edu.cn
[#]These authors contributed equally to this work

Received: 25 May 2026; Accepted: 31 July 2026; Published: 24 September 2026

ABSTRACT: Benzoquinone-derived organic cathodes are gaining prominence in rechargeable lithium-ion batteries owing to their rapid redox kinetics and sustainable origins. However, their practical application is severely limited by the high solubility of benzoquinone species in organic electrolytes, which leads to rapid capacity decay during cycling. Although polymerization can effectively suppress dissolution, the resulting polymers often suffer from poor electronic conductivity and low utilization of redox-active sites. Herein, a *p*-phenylenediamine-benzoquinone polymer (PPD-BQ) was synthesized and integrated with reduced graphene oxide (RGO) to fabricate self-supported flexible composite films through a simple one-pot strategy. The uniformly distributed polymer layers effectively prevent the restacking of RGO nanosheets, while the highly conductive RGO framework accelerates charge transport and suppresses polymer dissolution through strong interfacial interactions. Consequently, the PPD-BQ/RGO composite films demonsreste outstanding electrochemical properties, achieving a reversible capacity of 132 mAh g^{-1} at 2000 mA g^{-1}, with 73.0% capacity retention after 3000 cycles at 1500 mA g^{-1}. In addition, the composite films maintain 93.6% of their room-temperature capacity at 0°C in a DOL-based electrolyte, demonstrating excellent low-temperature electrochemical activity. This work presents a simple and scalable approach for fabricating flexible, high-performance organic electrode materials for sustainable energy-storage applications.

KEYWORDS: *p*-phenylenediamine-benzoquinone polymer; reduced graphene oxide; composite films; lithium-ion batteries; flexible electrode materials

1 Introduction

Owing to their superior energy density and extended service life, lithium-ion batteries have found widespread application in portable electronics, electric vehicles, and large-scale energy-storage systems [1–3]. At present, commercial cathode materials are still dominated by inorganic transition-metal compounds such as NCM and NCA [4]. However, concerns regarding limited resource availability, environmental impact, and cost have stimulated growing interest in sustainable electrode materials [5]. In this context, organic electrode materials have emerged as promising alternatives owing to their abundant raw material sources, structural tunability, fast redox kinetics, and potential for sustainable production [6,7]. Moreover, organic compounds composed of lightweight elements (C, H, O, and N) are highly attractive for next-generation energy-storage systems because they can potentially deliver high theoretical capacities and energy densities.

Among various organic electrode materials, benzoquinone (BQ) and its derivatives have attracted considerable attention due to their rapid redox kinetics, relatively high discharge potential (~2.7 V vs.

Li/Li$^+$), and high theoretical specific capacity (496 mAh g^{-1}) [8,9]. Nevertheless, the practical application of benzoquinone-based materials is severely hindered by their high solubility in conventional organic electrolytes, which leads to rapid capacity fading during cycling. Polymerization has been widely recognized as an effective strategy to suppress the dissolution of small organic molecules by incorporating them into insoluble polymer backbones [10]. However, to maintain a high specific capacity, the fraction of electrochemically inactive moieties in the polymer structure must be minimized. In this regard, direct polymerization of benzoquinone to form polybenzoquinone (PBQ) appears to be a straightforward solution. Unfortunately, PBQ generally exhibits limited reversible doping levels because severe Coulombic repulsion develops along the conjugated backbone during charge accumulation [11–14]. As a result, only a fraction of the redox-active sites can effectively participate in electrochemical reactions. Previous studies have suggested that separating benzoquinone units with non-conjugated linkers can alleviate this issue and improve the utilization of redox-active groups [15,16]. Nevertheless, such polymer structures often suffer from intrinsically low electronic conductivity, resulting in large Ohmic polarization and poor rate capability [17].

To address these challenges, a *p*-phenylenediamine-benzoquinone polymer (PPD-BQ) was designed and synthesized in this work. In this structure, benzoquinone units are spatially separated by *p*-phenylenediamine segments, which effectively suppresses the mutual electronic interference between adjacent quinone groups. Additionally, a one-pot, eco-friendly, and straightforward approach was devised to produce self-supported flexible PPD-BQ/reduced graphene oxide (PPD-BQ/RGO) composite films through the *in situ* polymerization of *p*-phenylenediamine (PPD) and benzoquinone (BQ) in the presence of graphene oxide (GO), followed by chemical reduction and vacuum filtration. The highly conductive RGO framework provides efficient electron-transport pathways, leading to significantly enhanced rate capability. Meanwhile, strong interactions between the polymer chains and RGO nanosheets effectively suppress the dissolution of PPD-BQ in organic electrolytes, thereby improving cycling stability. Benefiting from these structural features, the PPD-BQ/RGO composite films deliver nearly complete utilization of redox-active sites, achieving 99.4% of the theoretical capacity at 100 mA g^{-1}. Additionally, after 3000 cycles at 1500 mA g^{-1}, the composite films retain 73.0% of their initial capacity, and a reversible capacity of 132 mAh g^{-1} is still achieved at 2000 mA g^{-1}. Excellent low-temperature electrochemical activity is also demonstrated in a DOL-based electrolyte (DOL: 1,3-dioxolane), retaining 93.6% of the room-temperature discharge capacity when operated at 0°C. Thanks to their good flexibility and attractive electrochemical performance, the as-prepared composite films exhibit great potential for application in flexible and wearable energy-storage systems.

2 Results and Discussion

The synthetic routes of PPD-BQ and PPD-BQ/RGO are illustrated in Fig. 1a,b. PPD-BQ was synthesized through the polycondensation reaction between *p*-phenylenediamine (PPD) and benzoquinone (BQ), and the proposed polymerization mechanism is shown in Scheme S1. During the reaction, benzoquinone functions not only as a monomer but also as an oxidizing agent. Initially, BQ reacts with PPD via a 1,4-addition reaction to generate a secondary aminophenol intermediate. Subsequently, another BQ molecule oxidizes the aminophenol intermediate into a secondary amino-quinone species while being reduced to hydroquinone. These two processes proceed alternately, ultimately forming an insoluble polymer that precipitates from the aqueous solution (Fig. S1). In the presence of GO, the polymer preferentially nucleates and grows on the GO nanosheets, enabling the facile fabrication of PPD-BQ/RGO composites through a simple one-pot strategy (Fig. 1a). Moreover, by varing the feed ratio of the two monomers, the degree of

polymerization can be readily controlled [18]. Herein, the molar ratios of PPD to BQ were designed as 1:1, 1:2, 1:3, 1:5, and 1:10, respectively.

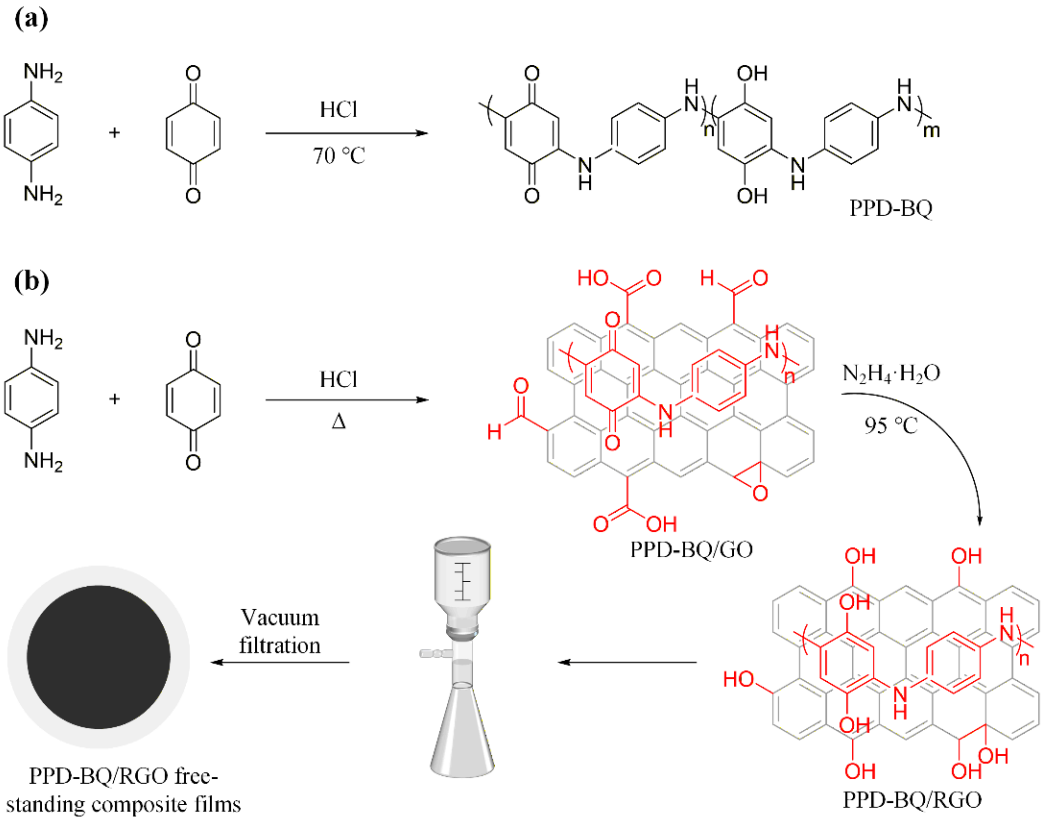

Figure 1: Schematic illustration of the synthesis procedures for (**a**) PPD-BQ and (**b**) PPD-BQ/RGO composite films.

Fourier-transform infrared (FTIR) spectroscopy was first employed to identify the functional groups of the polymer, as shown in Fig. 2a. For PPD-BQ-1, -2, -3, -5, and -10, the band located at 1629 cm^{-1} is attributed to the C=O stretching vibration. Compared with benzoquinone (1658 cm^{-1}), this peak exhibits a red shift of 29 cm^{-1}, which can be ascribe to C=O bond weakening induced by intermolecular and intramolecular hydrogen bonding between the C=O and –NH– groups in the polymer [19]. In the FTIR spectrum of PPD, the broad band in the range of 900–650 cm^{-1} corresponds to the out-of-plane deformation vibration of $–NH_2$ groups, whereas a new band appearing at 815 cm^{-1} in the polymer spectra is assigned to –NH– groups [20]. Furthermore, the appearance of the band at 1280 cm^{-1} corresponds to the stretching vibration of newly generated Ph–N bonds. These results collectively confirm the successful polymerization between PPD and BQ. Furthermore, the degree of polymerization is strongly dependent on the feed ratio, consistent with previous reports [18]. Compared with pure PPD, the characteristic band at 3370 cm^{-1} corresponding to the stretching vibration of $–NH_2$ groups is still observed in PPD-BQ-1, indicating a relatively low degree of polymerization at a higher PPD/BQ feed ratio (1:1). In contrast, for PPD-BQ-2, -3, -5, and -10, a distinct band at 3210 cm^{-1} assigned to –NH– stretching vibration becomes prominent, suggesting a higher degree of polymerization and increased molecular weight at lower PPD/BQ feed ratios.

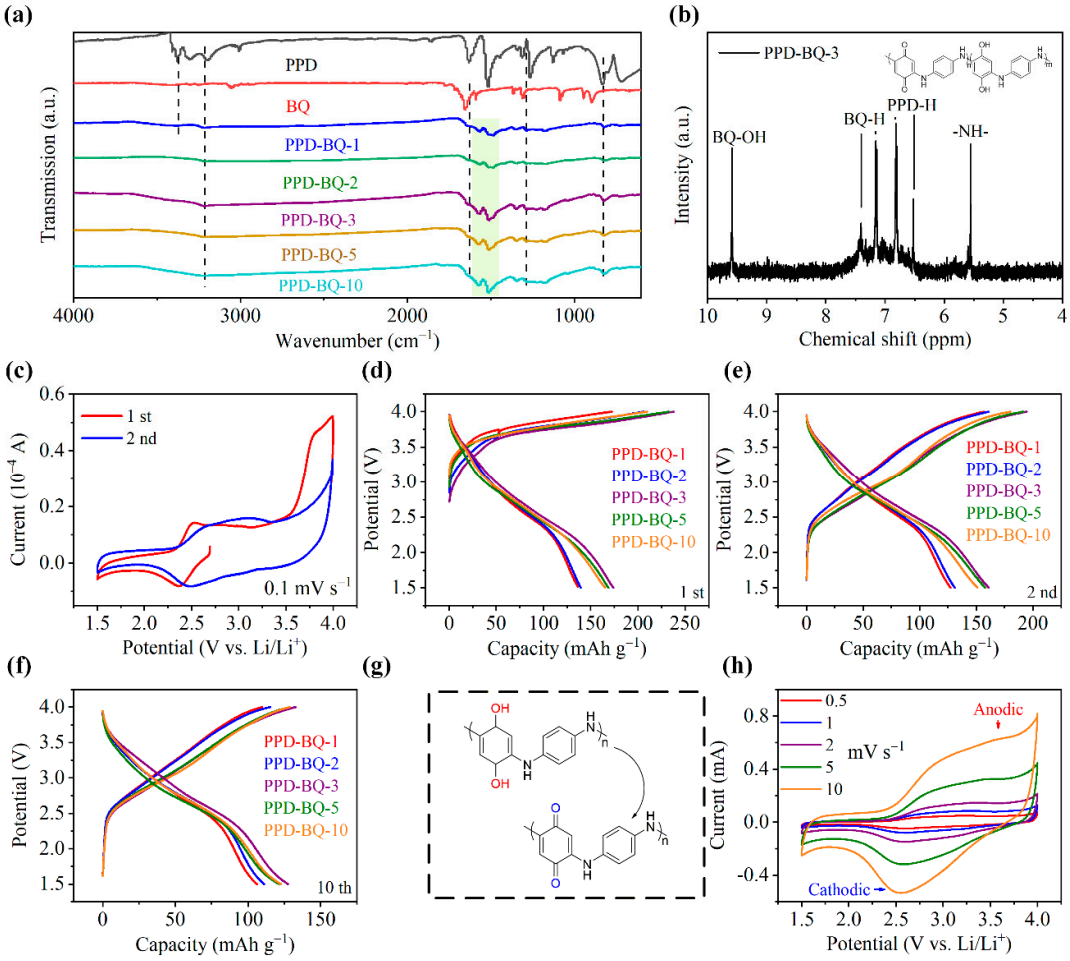

Figure 2: Characterization and electrochemical behavior of PPD-BQ. (**a**) FTIR spectra of PPD, BQ, and PPD-BQ polymers. (**b**) ^{1}H NMR spectrum of PPD-BQ-3. (**c**) CV curves of PPD-BQ-1 at a scan rate of 0.1 mV s^{-1} versus Li/Li$^+$. (**d**–**f**) Galvanostatic charge-discharge profiles of PPD-BQ at a current density of 100 mA g^{-1} during the (**d**) 1st, (**e**) 2nd, and (**f**) 10th cycles. (**g**) Electrochemical oxidation behavior of the polymers within 3.5–4.0 V. (**h**) CV curves of PPD-BQ-1 at scan rates of 0.5, 1, 2, 5, and 10 mV s^{-1} versus Li/Li$^+$.

While FTIR analysis confirms the formation of the polymer, it cannot distinguish whether PPD and BQ units are incorporated in the proposed coupled structure. To clarify the polymerization mode, a semi-quantitative analysis of the functional groups in PPD-BQ was carried out. To minimize the influence of terminal groups, PPD-BQ-3, which possesses a relatively high degree of polymerization, was selected for ^{1}H nuclear magnetic resonance (^{1}H NMR) characterization after dissolution in 0.6 mL of deuterated dimethyl sulfoxide ($(CD_3)_2SO$) (Fig. 2b). The signal at 5.55 ppm is assigned to the –NH– (P1), the two peaks at 6.52 and 6.81 ppm correspond to the aromatic hydrogen atoms on the phenylenediamine unit (P2), the signals at 7.15 and 7.41 ppm are attributed to the olefinic protons on the benzoquinone unit (P3), and the low-field peak at 9.58 ppm is assigned to the hydrogen atom of the non-oxidized phenolic hydroxyl group within the polymer chain segments. The integrated peak area ratio of P1:P2:P3 is calculated to be 1:2:1, which is generally consistent with the proposed polymerization pathway. These results further support the polymerization mechanism illustrated in Scheme S1.

To evaluate the electrochemical properties of the polymer, coin cells were fabricated with PPD-BQ-1 electrode sheets as the cathode and lithium metal as the anode. Two-electrode cyclic voltammetry (CV)

tests were conducted over a voltage range of 1.5–4.0 V at scan rates from 0.1 to 10 mV s^{-1} (Fig. 2c,h). In the initial cycle, the oxidation peak located at 2.52 V vs. Li/Li^+ and the corresponding reduction peak at 2.36 V are ascribed to the reversible interconversion between C–O and C=O groups, while the pronounced oxidation wave observed at 3.5–4.0 V is associated with the oxidation of hydroquinone units and rapidly weakens during subsequent cycles, consistent with previous reports [21]. In the second cycle, the redox peaks shift to 3.08/2.47 V vs. Li/Li^+, indicating the participation of nearly all reactive C=O groups, whereas only a fraction of these groups are electrochemically active during the initial cycle. In addition, the broader redox waves observed in the second cycle can be attributed to the heterogeneous chemical environments of benzoquinone groups along the polymer chains, which result in a distribution of electrode potentials [22,23].

Based on the CV curves of PPD-BQ-1, the electrochemical reaction mechanism of PPD-BQ in lithium-ion batteries can be inferred, as illustrated in Scheme S2. In non-protic electrolytes containing lithium ions, the quinone groups reversibly react with Li^+ and electrons during the discharge process to form lithium salts, while the lithiated species release lithium ions and electrons during charging to regenerate the quinone structure. Through this reversible conversion between quinone groups and their lithiated counterparts, PPD-BQ enables reversible lithium-ion storage. The theoretical specific capacity of PPD-BQ is calculated to be 253 mAh g^{-1} (Scheme S2). The CV behavior of PPD-BQ is in good agreement with the galvanostatic charge-discharge profiles (Fig. 2d–f), and the Coulombic efficiency gradually increases upon cycling, corresponding to the progressive oxidation of phenolic structures in PPD-BQ (Fig. 2g). Significantly, at 100 mA g^{-1}, PPD-BQ-3 delivers an initial charge capacity of 238 mAh g^{-1}, approaching the theoretical value and providing further support for the proposed electrochemical reaction mechanism.

Coin cells were assembled using PPD-BQ-1, -2, -3, -5, and -10 as the cathodes, lithium metal as the anode, and 1.0 M $LiPF_6$ in EC/DEC (1:1 by weight) containing 1% VC (EC: ethylene carbonate, DEC: diethyl carbonate, VC: vinylene carbonate) as the electrolyte to evaluate the electrochemical performance of the polymers. The rate performance of the PPD-BQ samples is presented in Fig. 3a–f. At current densities of 100, 200, 500, 1000, 2000, and 5000 mA g^{-1}, PPD-BQ-3 delivers reversible discharge capacities of 127.0, 111.0, 85.4, 70.3, 57.2, and 42.2 mAh g^{-1}, respectively. At the relatively low current density of 100 mA g^{-1}, the reversible capacity attains merely about 50% of the theoretical value. To gain insight into this inferior performance, we examined the morphology of the polymer particles by SEM (Fig. S2). Fig. S2a presents low-magnification SEM images (scale bar: 10 μm) of PPD-BQ-1, PPD-BQ-2, PPD-BQ-3, PPD-BQ-5, and PPD-BQ-10, clearly showing the overall morphology and extensive agglomeration of polymer particles across all samples. Fig. S2b provides corresponding high-magnification SEM images (scale bar: 2 μm), which further reveal the dense and irregular surfaces of the aggregated particles, indicating limited porosity and restricted accessibility of electrolyte to the internal redox-active sites. Such large polymer particles likely encapsulate numerous redox-active sites, hindering ion diffusion and resulting in incomplete utilization of the active material. The volcano-shaped trend observed among PPD-BQ samples with different feed ratios further supports this explanation. Excess BQ favors the 1,4-addition and subsequent oxidative polymerization, promoting polymer chain growth. At too low BQ ratios (PPD-BQ-1, -2), insufficient polymerization leads to substantial dissolution of oligomers and small molecules, resulting in low capacity. At a moderate BQ ratio (PPD-BQ-3), sufficient polymerization with appropriate molecular weight partially suppresses dissolution while maintaining a relatively loose packing structure that facilitates Li^+ diffusion, achieving the highest utilization of active sites. However, at too high BQ ratios (PPD-BQ-5, -10), although the polymerization degree is the highest and dissolution is most effectively suppressed, the polymer chains become overly densely packed, blocking ion transport channels and preventing some deep-seated active sites from participating in electrochemical reactions, leading to decreased capacity. When the current

density is returned to 100 mA g^{-1}, the specific capacities of PPD-BQ-1, -2, -3, -5, and -10 recover to 93.5, 95.6, 119.8, 104.8, and 109.5 mAh g^{-1}, corresponding to capacity retentions of 89.2%, 86.8%, 94.3%, 87.2%, and 87.2%, respectively. Nevertheless, the capacities decrease rapidly at high current densities, indicating poor rate capability arising from the intrinsically low electronic conductivity of PPD-BQ (<10^{-5} S cm^{-1}), which leads to significant Ohmic polarization within the electrodes.

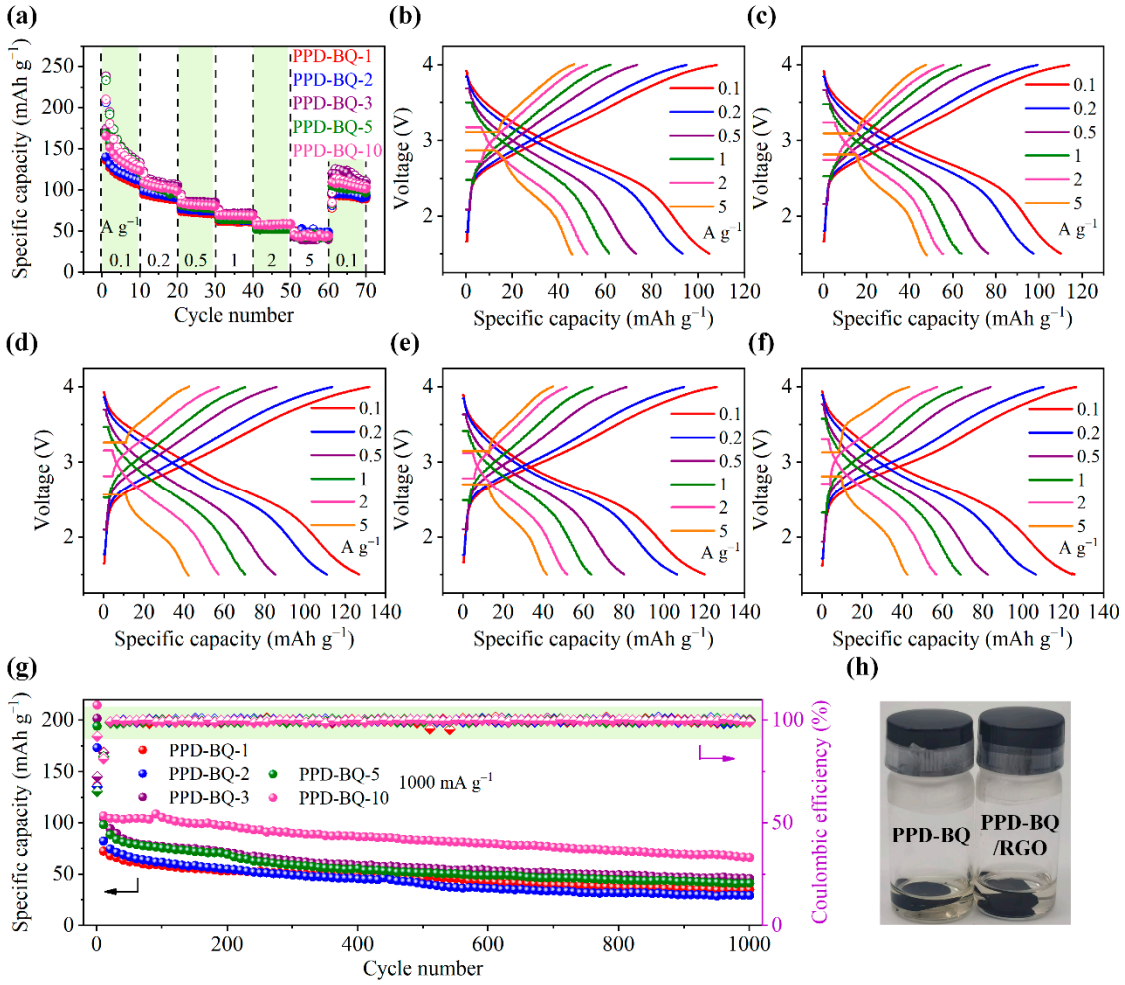

Figure 3: Electrochemical performance of PPD-BQ. (**a**–**f**) Rate performance of PPD-BQ polymers: (**a**) cycling capacities of PPD-BQ-1, -2, -3, -5, and -10 at different current densities; galvanostatic charge-discharge profiles of (**b**) PPD-BQ-1, (**c**) PPD-BQ-2, (**d**) PPD-BQ-3, (**e**) PPD-BQ-5, and (**f**) PPD-BQ-10. (**g**) Long-term cycling performance of PPD-BQ-1, -2, -3, -5, and -10 at 1000 mA g^{-1}. (**h**) Photographs of PPD-BQ-1 and PPD-BQ/RGO electrode films after immersion in electrolyte for 60 days.

For long-term cycling measurements, the coin cells were first activated for 10 cycles at 100 mA g^{-1} and subsequently cycled at 1000 mA g^{-1} (Fig. 3g). The initial discharge capacities of PPD-BQ-1, -2, -3, -5, and -10 are 72.3, 82.3, 104.4, 98.1, and 106.7 mAh g^{-1}, respectively. After 1000 cycles, the corresponding capacities decrease to 34.4, 29.0, 45.6, 40.6, and 66.1 mAh g^{-1}, with capacity retentions of 47.6%, 35.2%, 43.7%, 41.4%, and 61.9%, respectively. As the feed ratio of PPD to BQ decreases, the actual capacities of the polymers generally increase, and PPD-BQ-10 exhibits the best cycling stability among all samples. Nevertheless,

the overall cycling stability remains limited because PPD-BQ still possesses partial solubility in organic electrolytes, as evidenced by the immersion photographs shown in Fig. 3h and Fig. S3.

To overcome the limitations of pristine PPD-BQ, reduced graphene oxide (RGO) was introduced to construct PPD-BQ/RGO composite films through an *in situ* polymerization process (Fig. 1b). Previous studies have demonstrated that GO can oxidize hydroquinone into the corresponding benzoquinone structure [24]. Therefore, during the *in situ* growth of PPD-BQ on GO surfaces, GO can additionally function as an oxidizing agent, converting the products of the 1,4-addition reaction into amino-quinone structures and thereby promoting continuous polymerization. To optimize the synthesis conditions of the composite films, four parameters, including pH, the molar ratio of PPD/BQ/GO, reaction temperature, and reaction time, were systematically investigated through a series of control experiments (Table S1). At a current density of 100 mA g^{-1}, the electrochemical properties of the resulting samples were assessed using the total electrode mass as the active material mass (Fig. S4). Based on these results, the optimized composite films, denoted as PPD-BQ/RGO, were selected for subsequent characterization and electrochemical measurements.

Optical images of the PPD-BQ/RGO films are shown in Fig. 4a, demonstrating that the films can undergo large-angle bending without fracture, indicative of their excellent flexibility and self-supporting nature. The representative stress-strain curves in Fig. 4b further reveal favorable mechanical properties, with a Young's modulus of 59.4 ± 3.0 MPa and a tensile strength of 0.92 ± 0.04 MPa. Such mechanical robustness is beneficial for maintaining the structural integrity of the electrode during repeated charge-discharge processes. To verify that polymer growth in the presence of GO follows the proposed mechanism shown in Scheme S1, the chemical structures of the PPD-BQ/RGO composite films were further characterized by FTIR spectroscopy. As shown in Fig. 4c, both PPD-BQ and PPD-BQ/RGO exhibit a characteristic band at 1197 cm^{-1} assigned to C–O stretching vibration, while the bands in the range of 1500–1600 cm^{-1} corresponding to benzene ring vibrations in PPD-BQ/RGO originate from the combined contributions of PPD-BQ and RGO, confirming the successful formation of the composite structure. Notably, the characteristic C=O peak around 1620 cm^{-1} disappears in the spectrum of PPD-BQ/RGO, which is attributed to the simultaneous reduction of quinone groups into phenolic structures during the hydrazine reduction process of GO. According to thermogravimetric analysis (TGA) results (Fig. 4d), the PPD-BQ content in the composite film is determined to be 36.4 wt%, further confirming the successful incorporation of the polymer into the RGO framework.

The microscopic morphologies of RGO and PPD-BQ/RGO composite films were further investigated by SEM. As shown in Fig. S5 and Fig. 4e–g, hydrazine-reduced RGO consists of irregular particles formed by the aggregation of stacked RGO nanosheets [25,26]. By contrast, both the surface and cross-sectional SEM images of the PPD-BQ/RGO composite films reveal a well-defined two-dimensional lamellar architecture (Fig. 4e,g). The magnified SEM image in Fig. 4f reveals no obvious polymer particles on the surfaces of the RGO nanosheets. Consistently, no noticeable polymer aggregation is observed in the transmission electron microscopy (TEM) image (Fig. 4h), indicating that the polymer is uniformly distributed on the RGO nanosheets as thin layers. Such a morphology effectively prevents severe polymer aggregation and facilitates the exposure of electrochemically active sites. Brunauer-Emmett-Teller (BET) analysis (Fig. S6) shows that the PPD-BQ/RGO composite possesses a specific surface area of 11.67 m^2 g^{-1} and an average pore size of 13.2 nm. The interconnected lamellar structure is favorable for electron transport, while the relatively large surface area promotes electrolyte infiltration and ion diffusion within the electrode. The interlayer structure of the composite films was further examined by X-ray diffraction (XRD) (Fig. S7). PPD-BQ exhibits diffraction peaks at 20.1° and 26.3°, whereas RGO shows a characteristic diffraction peak at 23.2°. In the PPD-BQ/RGO composite, the original peaks at 20.1° and 23.2° disappear and a new peak emerges at approximately 21°, indicating an expanded interlayer spacing caused by the adsorption of

polymer chains on the RGO nanosheets, which is beneficial for lithium-ion insertion and extraction during electrochemical cycling.

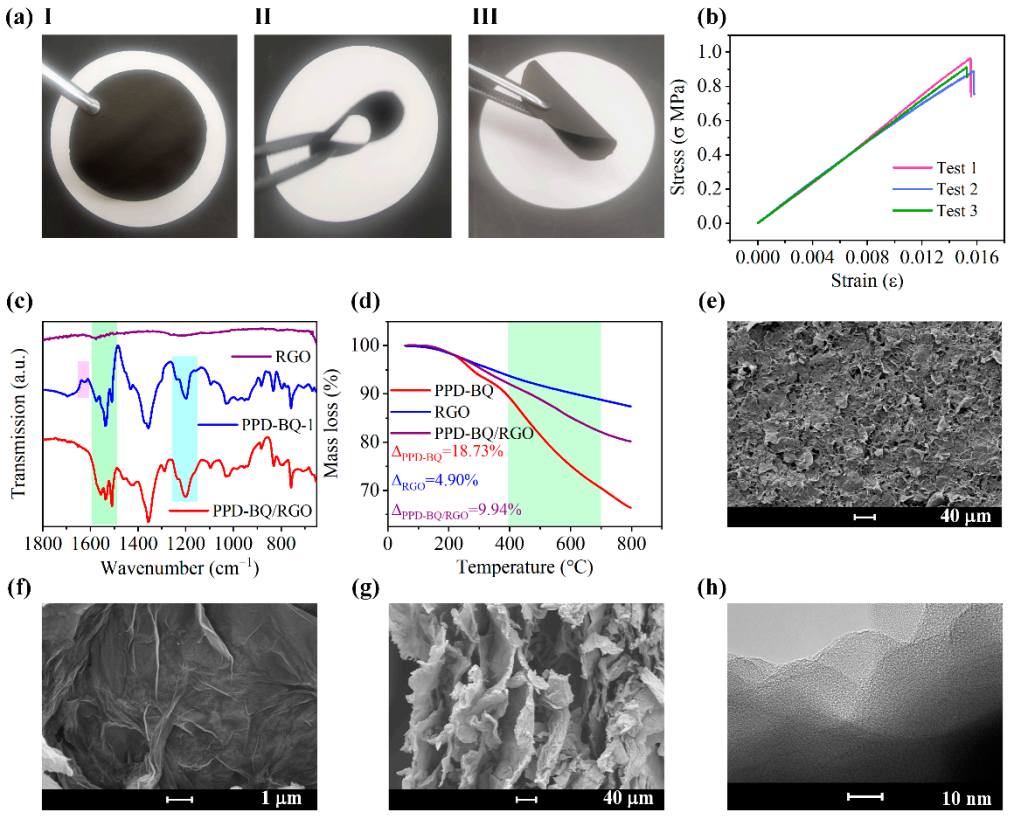

Figure 4: Characterization of PPD-BQ/RGO composite films. (**a**) Photographs of flexible PPD-BQ/RGO composite films. (**b**) Representative stress–strain curves of the composite films. (**c**) FTIR spectra of PPD-BQ-1, RGO, and PPD-BQ/RGO. (**d**) Thermogravimetric analysis (TGA) curves of PPD-BQ-1, RGO, and PPD-BQ/RGO measured under argon at a heating rate of 20°C min^{-1}. (**e**–**g**) SEM images of PPD-BQ/RGO composite films: (**e**,**f**) surface morphology and (**g**) cross-sectional morphology. (**h**) TEM image of PPD-BQ/RGO.

The electrochemical properties of the composite films were assessed using coin cells consisting of a PPD-BQ/RGO cathode, a lithium metal anode, and an electrolyte of 1.0 M $LiPF_6$ in EC/DEC = 1:1 by weight containing 1 vol% VC. As shown in Fig. S8, the CV curve of PPD-BQ/RGO exhibits a pair of redox peaks at 3.12/2.66 V vs. Li/Li$^+$, showing electrochemical behavior similar to that of pristine PPD-BQ at the same scan rate (0.1 mV s^{-1}). Notably, the current response of the composite films is significantly higher than that of the pristine polymer electrodes, which can be attributed to the substantially improved charge transport resulting from the incorporation of highly conductive RGO. In addition, the redox waves become broader and exhibit apparent capacitive characteristics, consistent with previous reports [27,28]. Therefore, directly using the oxidation peak potential (3.12 V) as the upper cutoff voltage would neglect part of the capacity contribution from the capacitive process. To determine an appropriate voltage window, cycling performances were further evaluated within voltage ranges of 1.5–3.8 V, 1.5–4.0 V, and 1.5–4.2 V at a current density of 1500 mA g^{-1} (Fig. S9). Among them, the 1.5–3.8 V window delivers the lowest initial discharge capacity of only 70 mAh g^{-1}, while the 1.5–4.2 V window provides a higher initial capacity but suffers from inferior cycling stability. Therefore, a voltage range of 1.5–4.0 V was selected for subsequent electrochemical measurements.

Fig. 5a,b presents the cycling performance of the PPD-BQ/RGO composite films. An initial specific capacity of 304.3 mAh g^{-1} is achieved at a current density of 100 mA g^{-1} (Fig. 5a, normalized to the mass of PPD-BQ polymer), exceeding the theoretical capacity of PPD-BQ (253 mAh g^{-1}). This additional capacity originates from the capacitive contribution and hydroxyl groups of RGO (Fig. S10). After subtracting the capacity contribution of RGO (30.3 mAh g^{-1}, based on the mass of RGO), the actual specific capacity of PPD-BQ is calculated to be 251.4 mAh g^{-1} (304.3 − (63.6/36.4) × 30.3 = 251.4, from TGA, Fig. 4d), corresponding to 99.4% utilization of the theoretical capacity and demonstrating the excellent electrochemical activity of the polymer. After 100 cycles, the residual discharge capacity remains as high as 254 mAh g^{-1}, corresponding to a capacity retention of 83.4%, indicative of favorable cycling stability. Prior to long-term cycling tests at high current densities, the composite films were pre-activated for 10 cycles at 100 mA g^{-1}. At 1000 mA g^{-1}, the initial discharge capacity amounts to 178.4 mAh g^{-1}, with 119 mAh g^{-1} remaining after 3000 cycles, which corresponds to a retention rate of 66.8%. Remarkably, the capacity decay rate gradually decreases after prolonged cycling, and during the final 2000 cycles the average capacity loss is less than 1.2 μAh g^{-1} per cycle. Such outstanding cycling stability can be attributed to the strong interactions between the polymer chains and RGO nanosheets, which effectively suppress the dissolution of active species into the electrolyte [28]. Furthermore, at a current density of 1500 mA g^{-1}, the composite films still retain 73.0% of their initial capacity after 3000 cycles, further demonstrating their excellent long-term electrochemical stability.

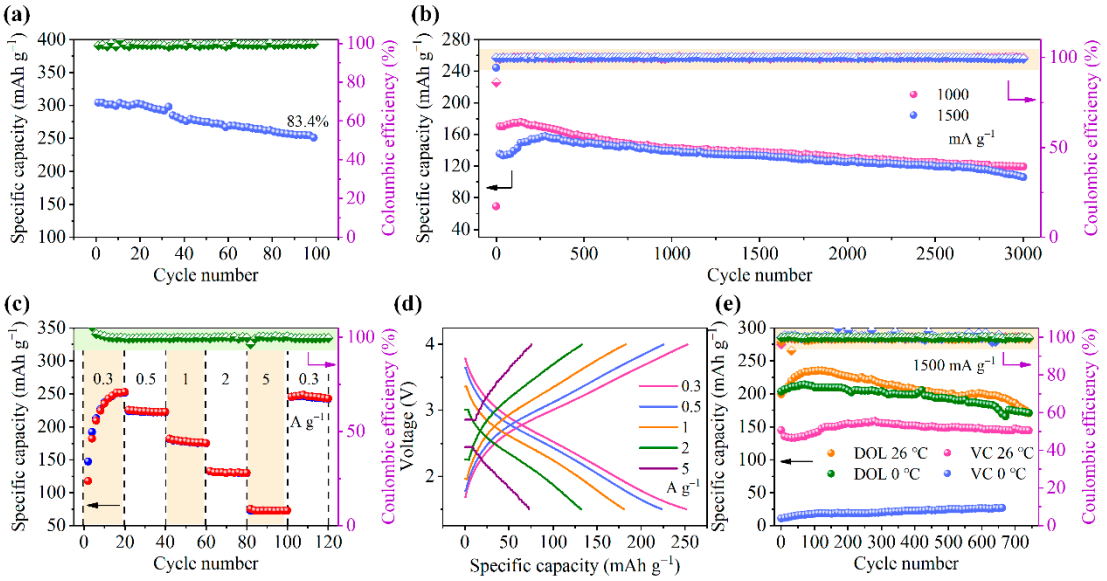

Figure 5: Electrochemical performance of PPD-BQ/RGO composite films. (**a**,**b**) Cycling performance at current densities of (**a**) 100 mA g^{-1} and (**b**) 1000 and 1500 mA g^{-1}. (**c**,**d**) Rate performance of PPD-BQ/RGO at various current densities. (**e**) Low-temperature electrochemical performance of PPD-BQ/RGO in different electrolytes, including 1.0 M $LiPF_6$ in EC/DEC = 1:1 by weight containing 1 vol% VC and 1.0 M LiTFSI in DOL/DME (1:1 by volume).

The PPD-BQ/RGO composite films also exhibit remarkable rate capability, as shown in Fig. 5c,d. Reversible capacities of 252, 224, 181, 132, and 73 mAh g^{-1} are achieved at current densities of 300, 500, 1000, 2000, and 5000 mA g^{-1}, respectively. Upon returning the current density to 300 mA g^{-1}, the capacity recovers to 245 mAh g^{-1}, equivalent to 97% retention, which demonstrates the excellent electrochemical reversibility of the composite films. The superior rate performance can be mainly attributed to the highly conductive RGO framework, which provides efficient electron-transport pathways and significantly accelerates charge-transfer processes within the electrode [29].

At 0°C, the PPD-BQ/RGO composite films exhibit markedly different electrochemical behaviors in different electrolytes (Fig. 5e). In the carbonate-based electrolyte, the initial discharge capacity is only 10.8 mAh g^{-1}, corresponding to 7.46% of the room-temperature capacity (144.8 mAh g^{-1}). In contrast, when a DOL-based electrolyte (1.0 M LiTFSI in DOL/DME = 1:1 by volume, LITFSI: lithium bis(trifluoromethanesulfonyl)imide, DOL: 1,3-dioxolane, DME: 1,2-dimethoxyethane) is employed, the initial discharge capacity at 0°C reaches 199.1 mAh g^{-1}, which corresponds to 93.6% of the room-temperature value (203.7 mAh g^{-1}). DOL and DME have much lower melting points (−95°C and −58°C, respectively) compared to EC (36°C) and DEC (−43°C). In addition, the DOL/DME mixture exhibits higher ionic conductivity at low temperatures than carbonate-based electrolytes (4.5×10^{-4} S cm^{-1} at −20°C) [30]. Therefore, the DOL-based electrolyte enables much better low-temperature performance. These results demonstrate the excellent low-temperature electrochemical activity of the composite films in suitable electrolyte systems and suggest that under low-temperature conditions, electrolyte optimization is critically important for maximizing the electrochemical performance of organic electrode materials.

3 Experimental Section

3.1 Materials

All chemicals were obtained from commercial suppliers and used directly without additional purification. Benzoquinone (97%), *p*-phenylenediamine (AR), ammonia (AR), hydrochloric acid (AR), and hydrazine hydrate (AR) were purchased from Xilong Chemical (China). Super-P, polyvinylidene fluoride (PVDF), Al foil, Li, and separator (Celgard 2500) were bought from Jinghong New Energy. Electrolytes (1.0 M $LiPF_6$ in EC/DEC = 1:1 by weight with 1 vol% VC, and 1.0 M LiTFSI in DOL/DME = 1:1 by volume) were purchased from Duoduo Chemical.

3.2 Synthesis of p-Phenylenediamine-Benzoquinone Polymer

A series of PPD-BQ polymers were synthesized by adding 250, 160, 120, 80, and 45 mg of *p*-phenylenediamine together with 250, 320, 360, 400, and 450 mg of benzoquinone, respectively, into a three-necked flask containing 30 mL of deionized water and 5 mL of hydrochloric acid (37%). The mixtures were reacted at 70°C for 24 h in an oil bath, yielding brownish-black suspensions. The products were collected by vacuum filtration, washed thoroughly with deionized water and ethanol, and dried under vacuum to obtain black powders. The corresponding yields were 23.6%, 52.5%, 56.3%, 59.4%, and 72.2%, denoted as PPD-BQ-1, PPD-BQ-2, PPD-BQ-3, PPD-BQ-5, and PPD-BQ-10, respectively.

3.3 Synthesis of PPD-BQ/RGO Composite Films

GO and RGO hydrogels were prepared according to a previously reported method [31]. For the synthesis of PPD-BQ/RGO composite films, a certain amount of *p*-phenylenediamine, benzoquinone, 20 g of GO aqueous dispersion (3 mg g^{-1}), and hydrochloric acid (37%) were sequentially added into a three-necked flask. The mixture was reacted at a designated temperature for a specific period to obtain a PPD-BQ/GO suspension. Then, 5 mL of ammonia solution together with 100 μL of hydrazine hydrate (80 wt%) was added, and the reaction proceeded at 95°C for 1.5 h. Upon cooling to ambient temperature, the resultant black flocculent precipitate was dispersed in 800 mL of deionized water and isolated via vacuum filtration using a PVDF membrane (220 nm), affording the PPD-BQ/RGO composite films. Detailed synthesis parameters are summarized in Table S1. Notably, PPD-BQ/RGO-A-1 was synthesized under argon atmosphere, while all other samples were prepared in air.

3.4 Assembly of Coin Cells

PPD-BQ-1, -2, -3, -5, and -10 were mixed with Super P and PVDF at a weight ratio of 3:6:1. The mixtures were ground for 10 min and dispersed in *N*-methyl-2-pyrrolidone (NMP) under stirring for 24 h to form homogeneous slurries. The resulting slurries were spread onto aluminum foil and then dried under vacuum at 80°C for 12 h to produce the cathodes. CR2032 coin cells were assembled in an argon-filled glovebox with H_2O/O_2 levels below 0.01 ppm. The electrodes and PPD-BQ/RGO composite films were punched into 12 mm disks and assembled using lithium metal as the anode and Celgard 2500 as the separator, with 80 μL of electrolyte for each cell. The PPD-BQ/RGO composite films have an average thickness of approximately 118 μm, an areal mass loading of 2.92 mg cm^{-2}, and a corresponding areal capacity of 0.323 mAh cm^{-2} based on the electrode mass. Two electrolytes were employed: 1.0 M $LiPF_6$ in EC/DEC = 1:1 by weight with 1 vol% VC, and 1.0 M LiTFSI in DOL/DME = 1:1 by volume. After assembly, the cells were allowed to rest for 5 h prior to electrochemical measurements. Unless otherwise specified, all electrochemical tests were carried out at 26°C.

3.5 Electrochemical Characterization

Electrochemical performances of the PPD-BQ electrodes and PPD-BQ/RGO composite films were evaluated using CR2032 coin cells. Cyclic voltammetry (CV) tests were conducted using a CHI 660E electrochemical workstation at scan rates of 0.1 to 10 mV s^{-1}. Galvanostatic charge–discharge measurements were conducted using a Wuhan LAND CT2001A battery testing system. PPD-BQ/RGO-A-1 to -A-6, -B-1 to -B-6, -C-1 to -C-3, and -D-1 to -D-4 were tested within a voltage range of 1.5–4.0 V at a current density of 100 mA g^{-1}, where the total electrode mass was used as the active material mass. Cycling stability tests were performed at 100, 1000, and 1500 mA g^{-1}, while rate performance was evaluated over a current density range of 100–5000 mA g^{-1}. Low-temperature electrochemical measurements were carried out at 0°C and 1500 mA g^{-1}.

3.6 Characterization

^{1}H NMR spectra were recorded on an Avance II 400 MHz spectrometer (Bruker, Germany). FTIR spectra were collected using a Nicolet iS10 spectrometer (Thermo Fisher Scientific, USA) in ATR mode with a diamond crystal. Morphologies were characterized by scanning electron microscopy (SU-70, Hitachi, Japan) and transmission electron microscopy (Talos F200, FEI, USA). Thermogravimetric analysis (TGA) was carried out on a Setsys Evolution 18 analyzer (Setaram Instruments, France). Specific surface area and pore-size distribution were measured using a 3H-2000PM2 surface area and porosity analyzer (Beishide Instrument Technology, China). X-ray diffraction (XRD) patterns were recorded on a D8 Advance diffractometer (Bruker, USA).

4 Conclusion

In this work, a *p*-phenylenediamine-benzoquinone polymer (PPD-BQ) with a theoretical specific capacity of 253 mAh g^{-1} was successfully designed and synthesized. Self-supported PPD-BQ/RGO composite films were further fabricated through a simple one-pot strategy combining *in situ* polymerization, chemical reduction, and vacuum filtration. The polymer was uniformly distributed on the surfaces of RGO nanosheets without obvious aggregation, effectively exposing electrochemically active sites and facilitating ion diffusion. Meanwhile, the highly conductive RGO framework accelerated charge transport and significantly improved the rate capability of the electrode. Strong interfacial interactions between the polymer chains and RGO nanosheets also effectively suppressed the dissolution of active species in organic electrolytes, leading to enhanced cycling

stability. As a result, the PPD-BQ/RGO composite films exhibited excellent electrochemical performance, achieving nearly complete utilization of redox-active sites at 100 mA g^{-1} and maintaining high reversible capacities over 3000 cycles at high current densities. In addition, excellent low-temperature electrochemical activity was achieved in a suitable electrolyte, where the discharge capacity at 0°C reached 93.6% of that at room temperature. This work provides a simple and scalable strategy for the development of flexible, sustainable, and high-performance organic electrode materials for advanced energy-storage applications.

Acknowledgement: The authors declare no additional acknowledgements beyond the funding statement below.

Funding Statement: The authors gratefully acknowledge the financial support from the National Natural Science Foundation of China (Grant No. 22179115, received by Hua Bai, https://www.nsfc.gov.cn).

Author Contributions: The authors confirm contribution to the paper as follows: study conception and design: Hua Bai, Zhouqishuo Cai; data collection: Zhouqishuo Cai, Yanan Zhao, Zewen Lin, Shumin Lin, Dan Zhong; analysis and interpretation of results: Zhouqishuo Cai, Donghua Liu; draft manuscript preparation: Zhouqishuo Cai, Hua Bai, Donghua Liu. All authors reviewed and approved the final version of the manuscript.

Availability of Data and Materials: The data and materials of this study are available upon reasonable request.

Ethics Approval: Not applicable.

Conflicts of Interest: Given his role as Editorial Boardr of this journal, Hua Bai had no involvement in the peer review of this article and had no access to information regarding its peer review. Full responsibility for the editorial process for this article was delegated to another journal editor. The authors declare no other conflicts of interest.

Supplementary Materials: The supplementary material is available online at https://www.techscience.com/doi/10.32604/jpm.2026.085943/s1.

References

1. Xie Y, Li W, Hu XS, Tran MK, Panchal S, Fowler M, et al. Coestimation of SOC and three-dimensional SOT for lithium-ion batteries based on distributed spatial-temporal online correction. IEEE Trans Ind Electron. 2023;70(6):5937–48. [CrossRef].
2. Ruan HK, He HW, Wei ZB, Quan ZY, Li YW. State of health estimation of lithium-ion battery based on constant-voltage charging reconstruction. IEEE J Emerg Sel Top Power Electron. 2023;11(4):4393–402. [CrossRef].
3. Jefferson TE, Rana S, Banerjee N. Lithium-ion batteries: a review of materials, design advances, sustainability challenges, and future prospects. Energy Storage. 2025;8(1):e70320. [CrossRef].
4. Celadon A, Sun HH, Sun SH, Zhang GX. Batteries for electric vehicles: technical advancements, environmental challenges, and market perspectives. SusMat. 2024;4(5):e234. [CrossRef].
5. Liu YH, Zhu YC, Appleberry M, Li F, Mu A, Jiao BL, et al. Toward more recyclable and sustainable lithium-ion batteries. ACS Appl Energy Mater. 2025;8(20):14902–18. [CrossRef].
6. Yang GJ, Zhu YX, Zhao Q, Hao ZM, Lu Y, Zhao Q, et al. Advanced organic electrode materials for aqueous rechargeable batteries. Sci China Chem. 2024;67(1):137–64. [CrossRef].
7. Li M, Ruan WH, Zhang MQ. Advances in organic polymer electrode materials for ion batteries: a comprehensive review. Polymer. 2024;307:127244. [CrossRef].
8. Li JB, Guan HR, Zhu SY, Liu B, Yao HY, Guan SW. Organic cathode with high-density active sites and extended π-conjugated structure for advanced high-performance lithium-ion batteries. J Colloid Interface Sci. 2025;696:137858. [CrossRef].
9. Sun HN, Li S, Tong YF, Sun JC, Lv LX, Jia JC, et al. Tetraamino-benzoquinone-based organic materials for advanced energy conversion and storage. Eur J Or Chem. 2026;29(15):e202501131. [CrossRef].

10. Yang JK, Zhao XR, Yang JX, Xu YH, Li YS. High-performance poly(1-naphthylamine)/mesoporous carbon cathode for lithium-ion batteries with ultralong cycle life of 45,000 cycles at −15°C. Adv Sci. 2023;10(23):2302490. [CrossRef].
11. Floris PS, Zozoulenko I, Rurali R. Doping efficiency of Poly(benzodifurandione) from first principles. J Phys Chem C. 2025;129(9):4354–7. [CrossRef].
12. Snook GA, Kao P, Best AS. Conducting-polymer-based supercapacitor devices and electrodes. J Power Sources. 2011;196(1):1–12. [CrossRef].
13. Muench S, Wild A, Friebe C, Häupler B, Janoschka T, Schubert US. Polymer-based organic batteries. Chem Rev. 2016;116(16):9438–84. [CrossRef].
14. Heinze J, Frontana-Uribe BA, Ludwigs S. Electrochemistry of conducting polymers-persistent models and new concepts. Chem Rev. 2010;110(8):4724–71. [CrossRef].
15. Song ZP, Qian YM, Liu XZ, Zhang T, Zhu YB, Yu HJ, et al. A quinone-based oligomeric lithium salt for superior Li-organic batteries. Energy Environ Sci. 2014;7(12):4077–86. [CrossRef].
16. Song ZP, Qian YM, Gordin ML, Tang DH, Xu T, Otani M, et al. Polyanthraquinone as a reliable organic electrode for stable and fast lithium storage. Angew Chem Int Ed. 2015;54(47):13947–51. [CrossRef].
17. Zhao Q, Zhu ZQ, Chen J. Molecular engineering with organic carbonyl electrode materials for advanced stationary and redox flow rechargeable batteries. Adv Mater. 2017;29(48):1607007. [CrossRef].
18. Song ZY, Zhu DZ, Li LC, Chen T, Duan H, Wang ZW, et al. Ultrahigh energy density of a N, O codoped carbon nanosphere based all-solid-state symmetric supercapacitor. J Mater Chem A. 2019;7(3):1177–86. [CrossRef].
19. Sieuw L, Jouhara A, Quarez É, Auger C, Gohy JF, Poizot P, et al. A H-bond stabilized quinone electrode material for Li-organic batteries: the strength of weak bonds. Chem Sci. 2019;10(2):418–26. [CrossRef].
20. Shi YQ, Yang JK, Yang JX, Wang ZP, Chen ZF, Xu YH. Quinone-amine polymer nanoparticles prepared through facile precipitation polymerization as ultrafast and ultralong cycle life cathode materials for lithium-ion batteries. Adv Funct Mater. 2022;32(21):2111307. [CrossRef].
21. Song ZP, Qian YM, Zhang T, Otani M, Zhou HS. Poly(benzoquinonyl sulfide) as a high-energy organic cathode for rechargeable Li and Na batteries. Adv Sci. 2015;2(9):1500124. [CrossRef].
22. Yoo E, Kim J, Hosono E, Zhou H, Kudo T, Honma I. Large reversible Li storage of graphene nanosheet families for use in rechargeable lithium ion batteries. Nano Lett. 2008;8(8):2277–82. [CrossRef].
23. Liu YH, Xue JS, Zheng T, Dahn JR. Mechanism of lithium insertion in hard carbons prepared by pyrolysis of epoxy resins. Carbon. 1996;34(2):193–200. [CrossRef].
24. Sridhar V, Lee I, Chun HH, Park H. Hydroquinone as a single precursor for concurrent reduction and growth of carbon nanotubes on graphene oxide. RSC Adv. 2015;5(84):68270–5. [CrossRef].
25. Sahito IA, Sun KC, Arbab AA, Qadir MB, Jeong SH. Integrating high electrical conductivity and photocatalytic activity in cotton fabric by cationizing for enriched coating of negatively charged graphene oxide. Carbohydr Polym. 2015;130:299–306. [CrossRef].
26. Wang S, Wang X, Sun CL, Wu ZS. Room-temperature fast assembly of 3D macroscopically porous graphene frameworks for binder-free compact supercapacitors with high gravimetric and volumetric capacitances. J Energy Chem. 2021;61:23–8. [CrossRef].
27. Cai ZQS, Zhang JM, Lin ZW, Zhao YA, Yang QQ, Qiu XW, et al. Low-cost p-benzoquinone-formaldehyde polymer/reduced graphene oxide composite films as a cathode material for rechargeable lithium-ion batteries. J Mater Chem A. 2024;12(19):11439–47. [CrossRef].
28. Wu HZ, Luo SH, Wang HB, Li L, Gao XN, Zhang ZG, et al. An ultra-stable sodium dual-ion battery based on S/Se co-doped covalent organic framework anode with 12,000 cycles under lean electrolyte. Energy Storage Mater. 2025;75:104052. [CrossRef].
29. Wu HZ, Yuan WH, Li L, Gao XN, Zhang ZG, Qian Y. Ultra-high capacity and stable dual-ion batteries with fast kinetics enabled by HOF supermolecules derived 3D nitrogen-oxygen co-doped nanocarbon anodes. Adv Funct Mater. 2024;34(46):2406540. [CrossRef].
30. He YY, Shan XY, Li Y, Li ZX, Li L, Zhao S, et al. *In-situ* formation of quasi-solid polymer electrolyte for wide-temperature applicable Li-metal batteries. Energy Storage Mater. 2024;68:103281. [CrossRef].
31. Chen J, Yao BW, Li C, Shi GQ. An improved hummers method for eco-friendly synthesis of graphene oxide. Carbon. 2013;64:225–9. [CrossRef].